Pergamon

Int. J. Solids Structures Vol. 34, No. 30, pp. 3977–4004, 1997

0020-7683/97 $17.00 + .00

PII: S0020-7683(96)00228-4

NUMERICAL SIMULATION OF IMPACT LOADED STEEL BEAMS AND THE FAILURE CRITERIA

JI-LIN YU†
Department of Modern Mechanics, University of Science and Technology of China, Hefei, Anhui 230026, P. R. China

and

NORMAN JONES
Impact Research Centre, Department of Mechanical Engineering, University of Liverpool, Liverpool L69 3GH, U.K.

(*Received* 20 *December* 1995; *in revised form* 25 *October* 1996)

Abstract—The experimental results for clamped mild steel beams under impact loading reported by Yu and Jones (Yu, J. L. and Jones, N. (1991) Further experimental investigations on the failure of clamped beams under impact loads. *International Journal of Solids and Structures* **27**, 1113–1137) are simulated numerically using the finite-element code ABAQUS with plane stress elements. General observations are presented, including the effect of flexural wave propagation during the early stage of motion and the influence of material strain rate sensitivity and inertia effects on the structural response. The critical conditions for the beams during the response are revealed and various possible failure criteria are examined and discussed by comparing the experimental and numerical results. © 1997 Elsevier Science Ltd.

NOMENCLATURE

B	beam breadth
D	material constant in the Cowper–Symonds eqn (1)
G	striker mass
H	beam thickness
M	bending moment
M_0	$\sigma_y BH^2/4$
N	membrane force
N_0	$\sigma_y BH$
P	hydrostatic pressure, $P = -(\sigma_{xx}+\sigma_{yy}+\sigma_{zz})/3$
Q	transverse shear force
Q_0	$\sigma_y BH/\sqrt{3}$
T	time when the maximum deflection is reached
V_0	initial impact velocity
W	maximum transverse deflection
W_f	deflection at the onset of fracture observed by high-speed photography
W_I	displacement of the impact point
W_L	displacement of the point on the lower surface underneath the striker
W_{Lf}	value of W_L at the onset of fracture observed by high-speed photography
W_{Lp}	permanent value of displacement of W_L measured after a test
$W_{\max}$	maximum transverse deflection reached during the response in a numerical simulation
W_p	permanent maximum deflection measured after a test or estimated after unloading in a numerical simulation
W_s	depth of indentation at the impact point
d	distance from the impact point
e	engineering strain
e_f	engineering rupture strain
$2l$	beam span
l_1	distance of the load point to the nearest support
p	material constant in the Cowper–Symonds eqn (1)
s	engineering stress
t	time

† Visiting Professor at the University of Liverpool supported by the Royal Society and the Chinese Academy of Science.

x	axial coordinate
α	strain-rate hardening factor, $\alpha = 1+(\dot{\varepsilon}/D)^{1/P}$, where $\dot{\varepsilon}$ is taken to be the maximum value during the main response for individual specimen
γ	maximum shear strain defined by eqn (6)
ε	true strain
$\dot{\varepsilon}$	strain rate
ε^p_{eq}	equivalent plastic strain
ε_f	rupture strain, $\varepsilon_f = 0.83$
ζ	plastic strain energy density
η	dimensionless plastic strain energy density with respect to the static plastic strain energy density at rupture strain, i.e., 518 MJ/m^3, which is obtained by integrating the static true stress–strain curve up to the rupture strain (Yu and Jones, 1991)
λ	characteristic length scale for the strain energy density criterion
ξ	yield index, $\xi = \lvert M/M_0\rvert\sqrt{1-(Q/Q_0)^2+(N/N_0)^2+(Q/Q_0)^2}$
ξ_f	failure index, similar to ξ except that σ_f instead of σ_y is used in calculating N_0, M_0 and Q_0
σ	true stress
σ_f	static rupture stress, $\sigma_f = 784$ MPa
σ_{Mises}	Mises equivalent stress
σ_{Tresca}	Tresca equivalent stress
σ_y	static yield stress, $\sigma_y = 259$ MPa
$\sigma_0(\varepsilon)$	fictitious static stress–strain curve (Yu and Jones, 1991)
τ_f	static shear stress at failure in tensile tests, $\tau_f = \sigma_f/2$
τ_y	static shear stress at yield in tensile tests, $\tau_y = \sigma_y/2$.

1. INTRODUCTION

During the last decade, the topics of structural crashworthiness and failure have become one of the most active topics of research in impact dynamics and an area of increasing interest to designers in many industries (Jones and Wierzbicki, 1993). Although the deformation of structures, which are subjected to dynamic loads producing inelastic strains, has been investigated extensively (Jones, 1989a, b), the dynamic failure of structures, as a result of severe deformations and material rupture, is not well understood. The main difficulty lies in the fact that deformation is a global response, while failure is a local phenomenon. Detailed information on the mechanical state in the vicinity of a failure site is required for a failure analysis and some methods, which are used in the analysis of global response of structures under dynamic loading with great success, are not suitable for a local analysis.

An elementary rigid–plastic method was developed by Jones (1976) in order to explain the three failure modes obtained in the experimental results reported by Menkes and Opat (1973) on aluminium alloy beams loaded impulsively. The large ductile deformations associated with dynamic loads not causing any material failure is known as mode I response, and this behaviour has been studied extensively. However, as the impulsive loads are increased, then material rupture may occur at the supports, which is known as a mode II failure mode. Transverse shear failure may occur at the supports for even larger impulsive loads which is known as a mode III failure and occurs for relatively small transverse displacements of a beam. This method of analysis has been found useful for several other structures and has given surprisingly good agreement with experimental results, particularly when considering the simplicity of the method, which, nevertheless, captures the essential features of behaviour.

The energy density failure criterion is a promising method for predicting the dynamic inelastic failure of structures because it is, potentially, a universal criterion, but it has only been examined for some beam (Shen and Jones, 1992, 1993a) and plate (Shen and Jones, 1993b) problems. Several aspects of this method require further study, along with an examination of the accuracy of other criteria for the dynamic inelastic failure of structures.

Finite-element methods have been used by several authors to simulate the inelastic response of structures (Clift *et al.*, 1987, 1990; Yu and Jones, 1989). For example, a range of simple metal forming operations was simulated numerically by Clift *et al.* (1987, 1990) who compared the fracture initiation sites predicted by nine different fracture criteria with the experimental observations. It was observed that only the critical generalised plastic work density criterion predicted successfully the sites found experimentally in all of the metal forming operations. A numerical simulation of clamped aluminium alloy beams impacted transversely by a mass at different locations on the span, reported by Yu and

Table 1. Experimental details of mild steel beams in Yu and Jones (1991) ($2l = 101.6$ mm)

Specimen number	H (mm)	B (mm)	l_1 (mm)	V_0 (m/s)	W_p (mm)	W_{Lp} (mm)	W_f (mm)	W_s (mm)	Failure mode	Comments
SB10	6.29	10.21	50.8				20.1			quasi-static
SB09	6.29	10.10	50.5	10.5	20.90	20.90		0.5	I	
SB08	6.20	10.13	49.9	10.6			21.8		II	just broken
SB06	6.20	10.16	50.8	11.5			22.8		II (?)	broken
SB03	6.19	10.22	25.4†			$W_{Lf} = 16.46$				quasi-static
SB07	6.20	10.17	25.4	8.8	14.52	13.90		1.1	II + III	crack and necking
SB05	6.23	10.06	25.4	8.2			15.0		II + III/III (?)	broken
SB04	6.30	10.18	25.4	10.1			16.0		II + III/III (?)	broken

†Load position moved 0.4 mm towards the mid-span during the response.

Jones (1989), showed that the mode II failure of the beams could be predicted by the maximum tensile strain criterion, or equivalently, the overall rotation angle. These studies have shown the potential of combining numerical investigations with experimental tests to obtain the criterion which controls a structural failure.

This present study is part of a systematic research programme on the dynamic inelastic failure of structures and is a continuation of the previous careful experimental investigation reported by Yu and Jones (1991) on clamped beams struck by a solid mass, G, travelling with an initial velocity, V_0. The mechanical properties of the mild steel and aluminium alloy specimen material were obtained from both quasi-static and dynamic uniaxial tensile tests. The mild steel beams were loaded at the mid-span and the one quarter-span positions. Three beams were loaded dynamically by a mass having different impact velocities and one beam was loaded quasi-statically at each impact position. The experiment details of the mild steel beams are listed in Table 1.

In this paper, a numerical simulation is presented for the experimental tests on the mild steel beams reported by Yu and Jones (1991). The actual experimentally determined material properties are used in the finite-element models and the global response and strain history are compared with the experimental data. A numerical simulation for the quasi-static tensile tests of the mild steel material is also conducted. Detailed information on the dynamic inelastic response of the beams related to the structural failure is obtained. Through the combined study of the experimental investigation by Yu and Jones (1991) and the present numerical simulation, the reliability of both numerical and experimental results is confirmed and the critical conditions for the beams during the response are revealed. Various possible failure criteria are examined. Some general observations, including the effect of flexural wave propagation during the early stage of motion and the influence of material strain rate sensitivity on the structural response, are also presented.

2. METHOD OF NUMERICAL SIMULATION

In the experimental study reported by Yu and Jones (1991), flat beam specimens, made from mild steel with a nominal cross-sectional area $B \times H = 10.16 \times 6.35$ mm^2, were fully clamped across a span of $2l = 101.6$ mm.

The numerical simulations were conducted using the finite-element code ABAQUS. 2-D finite element models, as shown in Fig. 1, were constructed to simulate the dynamic or quasi-static response of the beams. 8-node biquadratic isoparametric plane stress elements with reduced integration were used for the beam and the striker. Interfacial elements were employed to allow the two bodies to separate or to remain partially or fully in contact with a possible small relative sliding without frictional effects. The striker was simplified and reduced to a short cuboid with large density but having the same mass as that used in the experiments ($G = 5$ kg) and was assumed elastic with the Young's modulus properly adjusted to accommodate the stress wave effect. The number of elements used in a dynamic analysis is 98 for the beams struck at the mid-span (symmetric case) and 174 for those struck at the one quarter-span position with the number of nodes being 362 and 624, respectively.

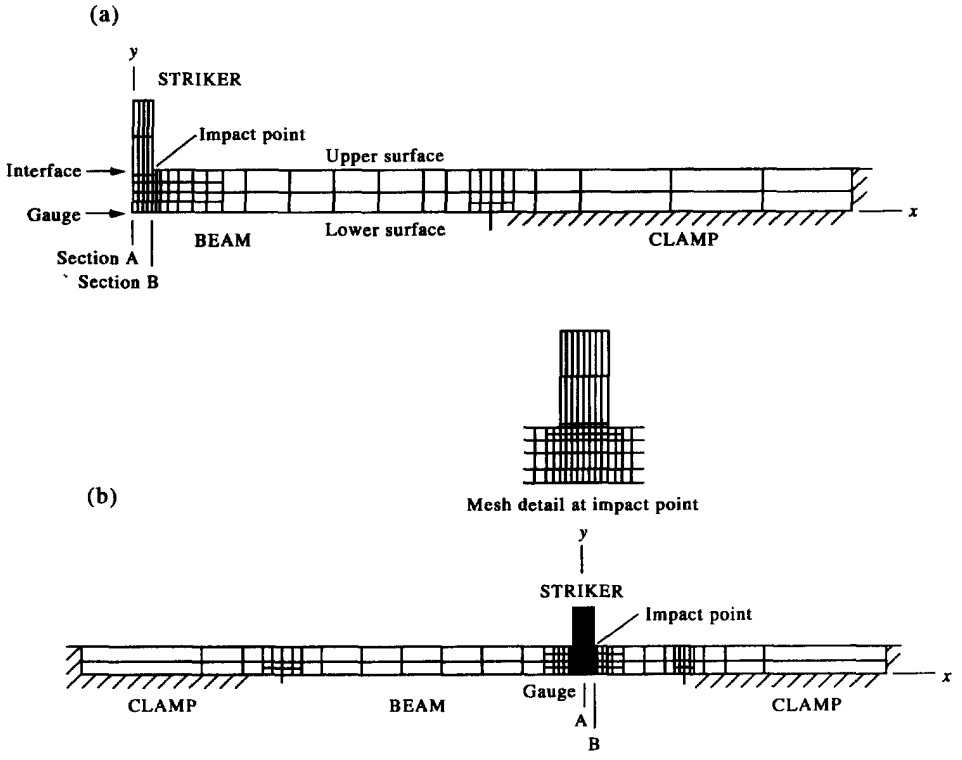

Fig. 1. Mesh for beams impacted (a) at the mid-span (symmetrical), and (b) at the one quarter-span position.

It was observed that the large deformations of the beams in the experimental study caused the upper surfaces of a beam to lose contact with the supports. Thus, the clamping conditions were modelled in the numerical simulation by fixing the two end faces and that part of the lower surface in contact with the supports, while the upper surface remained free. It should be noted that three-dimensional effects were not considered since plane stress elements were used in the simulation. This simplification will cause some error in the local stress and strain distributions. The most severely deformed location on a beam is near to the corner of the striker, because when a beam deforms, only a small part of the plane end of a striker contacts the beam surface. The node on a beam connected to the corner of the striker is referred to as the impact point hereafter. In considering the possibility of mesh-sensitivity and relatively lower accuracy of data at nodes extrapolated from the integration points, identical mesh structures near the impact point for the two sets of beams were adopted to give a reliable comparison.

True strain and true stress were used as the strain and stress measurements and geometrical nonlinearity was taken into account. Incremental elastic–plastic material properties with isotropic strain hardening and strain-rate hardening were used for the mild steel beams. The von Mises' yield criterion was assumed for the material data obtained from Yu and Jones (1991) which were obtained from the same block of material as used for the beam specimens. The material property is described by the Cowper–Symonds equation for the uniaxial case as

$$\sigma = \sigma_0(\varepsilon)[1 + (\dot{\varepsilon}/D)^{1/P}] \tag{1}$$

with $D = 1.05 \times 10^7\ \mathrm{s}^{-1}$ and $p = 8.30$, and a fictitious static stress–strain curve $\sigma_0(\varepsilon)$. No failure criterion was incorporated in the numerical code.

The dynamic analysis used direct implicit time integration with an automatic time step control based on the half-step residual concept. Newton's method was employed for solving the nonlinear equilibrium equations using the Hilber–Hughes–Taylor operator with the

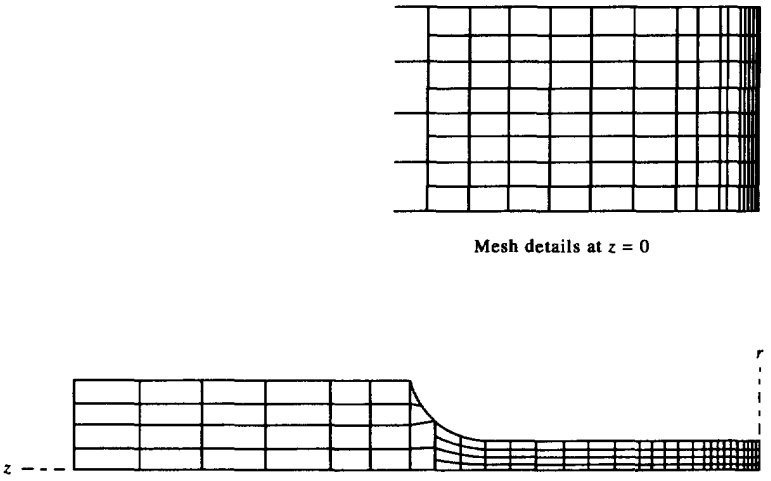

Fig. 2. Mesh for cylindrical tensile specimens.

artificial damping parameter $\alpha = -0.05$ and Newmark's formulae were used for the displacement and velocity integration.

In the quasi-static loading cases, the striker and the interfacial elements are replaced by a rigid surface and conjugate rigid surface elements. The same material properties including strain-rate sensitivity were used. However, the inertial effect was neglected. The load was applied through the rigid surface with a loading rate of 0.4 kN/min, which corresponds to a test duration of about an hour and results in an average strain rate of 2.4×10^{-4} s^{-1}, approximately. Newton's method was used in the quasi-static analysis to solve the equilibrium equations and the time increment was automatically adjusted according to the convergence rate. For more details of the numerical procedure the reader is referred to ABAQUS Theory and User's Manuals (Hibbitt, Karlsson and Sorensen, Inc., 1994a, b).

A numerical simulation for the quasi-static tensile test was also conducted in order to explore the stress, strain and strain energy distribution in the neck at failure as well as the error in the rupture stress caused by neglecting the three-dimensional effect and the increase of strain-rate in the neck. Standard cylindrical tensile specimens with a nominal diameter of 5 mm were used in the experimental tests. Correspondingly, a mesh was generated using 8-node biquadratic axisymmetric elements with reduced integration, as shown in Fig. 2. To initiate necking, the initial 2.5 mm radius of the specimen near the centre was reduced gradually by 1 μm (initial imperfection). The loading of the tensile specimens was displacement controlled with two loading speeds corresponding to nominal strain rates of 0.0012 s^{-1} and 0.012 s^{-1}, as used in the experiments.

In order to assess the accuracy of the numerical model, a coarse mesh was also used for specimen SB08 by doubling the length in the x-direction of the elements near the centre of the lower surface, where the strain gauge was located. It was found that the maximum strain on the lower surface underneath the striker is lower than that obtained using a finer mesh, especially during the second half of the response when the strain gradient is very high in that area. However, the strain history for the strain gauge record, which is calculated by averaging the strain values at relevant nodes, is identical. Also, there is no difference in the global response.

To investigate the influence of the elastic modulus of the simplified striker on the response of the beam, two values of the Young's modulus were used, namely, $E = 1.0 \times 10^9$ MPa (used only for the purpose of comparison) which represents a nearly rigid solid, and $E = 5.0 \times 10^5$ MPa which will produce the same effect as a longitudinal stress wave travelling along a steel striker of length 228 mm. This later case will also produce local deformation at the impact surface of the striker since this value is only one and a half times larger than that for steel. It transpires from a comparison of these two sets of results that the effect of

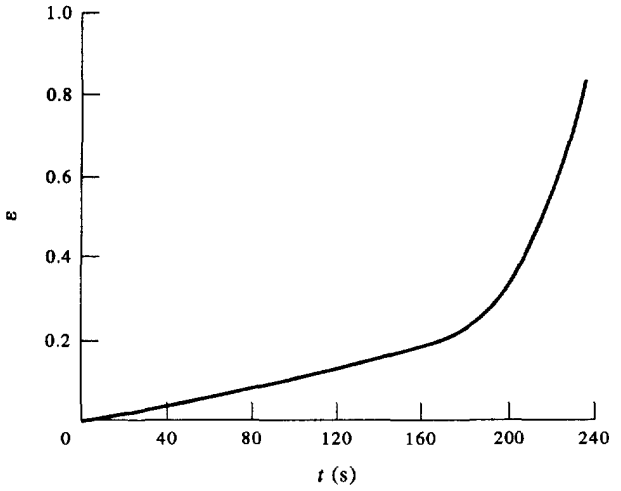

Fig. 3. History of the true strain, calculated from the change of the cross-section area, for a tensile specimen with $\dot{\varepsilon} = 0.0012\ s^{-1}$.

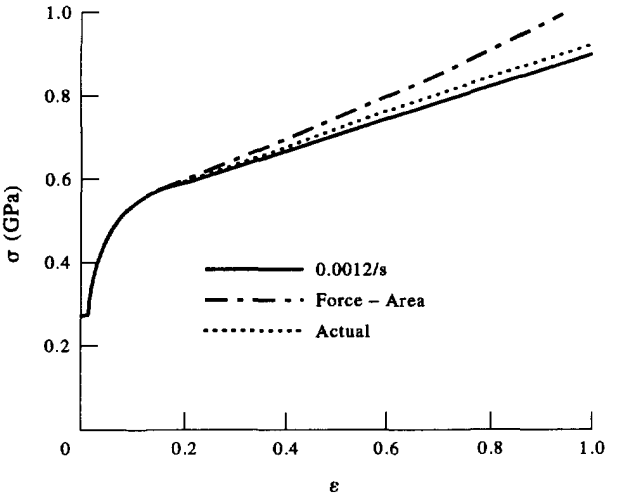

Fig. 4. Stress vs strain curves of a tensile specimen with $\dot{\varepsilon} = 0.0012\ s^{-1}$.

the stress wave in the striker on the response of the beam is negligible though there are slight differences for the values at the impact point and the contact force-time history.

3. NUMERICAL SIMULATION OF TENSILE TESTS

The history of the true strain, calculated from the change of the cross-sectional area, for the tensile specimen with a nominal strain rate of $0.0012\ s^{-1}$, is shown in Fig. 3. It transpires that, when necking occurs, the strain rate at the neck increases significantly. Consequently, the actual stress after necking is higher than that calculated using the nominal strain rate. On the other hand, due to three-dimensional effects, the stress calculated using the one-dimensional theory is higher than the equivalent stress, i.e., the Mises stress. It is found that the rupture stress calculated from the axial force and the area of the cross-section, or from the averaged axial stress using $\varepsilon_f = 0.83$ according to the experimental results reported by Yu and Jones (1991), is about 12% higher than that for the material at the same strain rate, as shown in Fig. 4. However, an increase of only 2.6% or 3.3% in the rupture stress due to the strain-rate effect at the strain-rate of $0.0012\ s^{-1}$ and $0.012\ s^{-1}$, respectively, is found when the Mises stress and equivalent plastic strain are used. This means that the main deviation of the rupture stress, when obtained by dividing the force

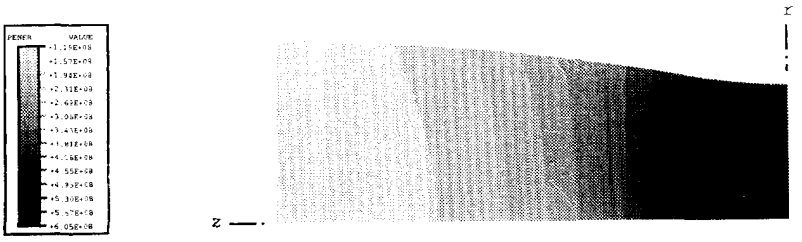

Fig. 5. Distribution of the plastic strain energy density at $\varepsilon = \varepsilon_f$ in the neck of a tensile specimen with $\dot{\varepsilon} = 0.0012\ s^{-1}$.

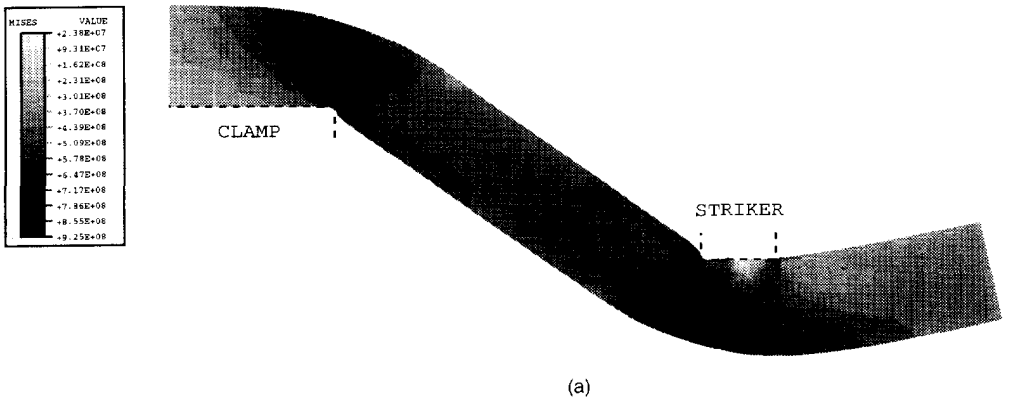

(a)

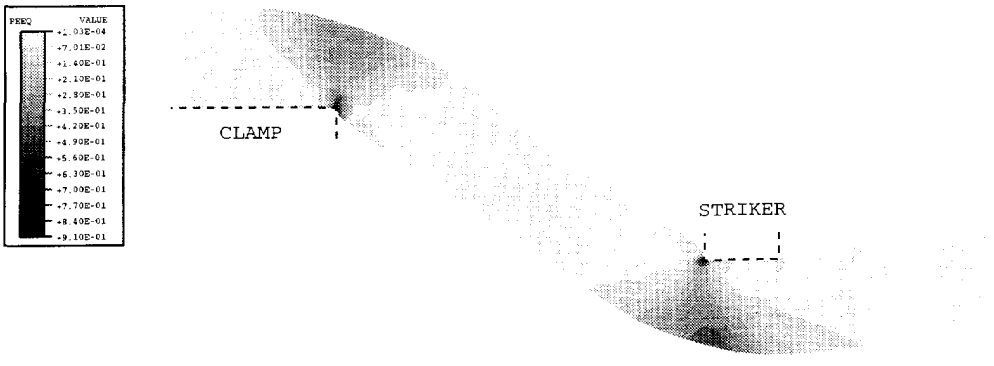

(b)

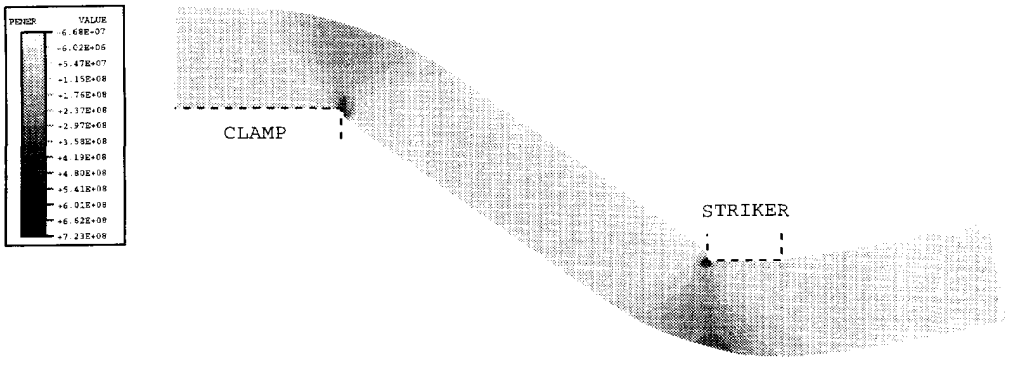

(c)

Fig. 15. Distribution of (a) Mises stress, (b) equivalent plastic strain, and (c) plastic strain energy density for specimen SB07 at $t = 2.86$ ms.

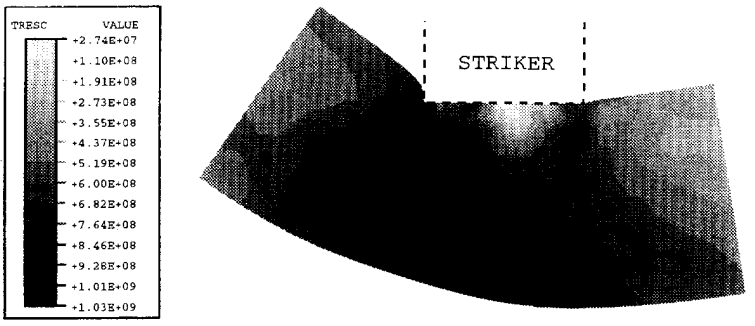

Fig. 16. Contour of Tresca stress for specimen SB07 at $t = 2.86$ ms.

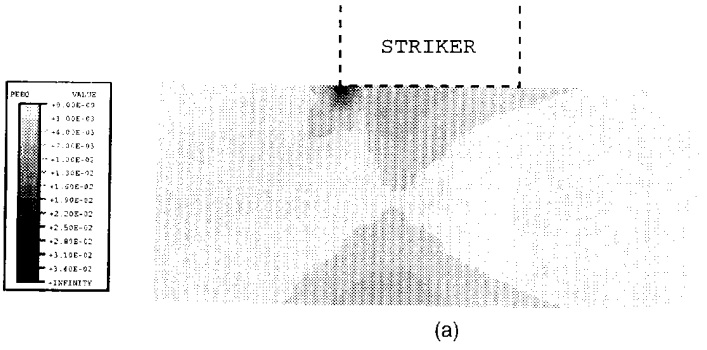

(a)

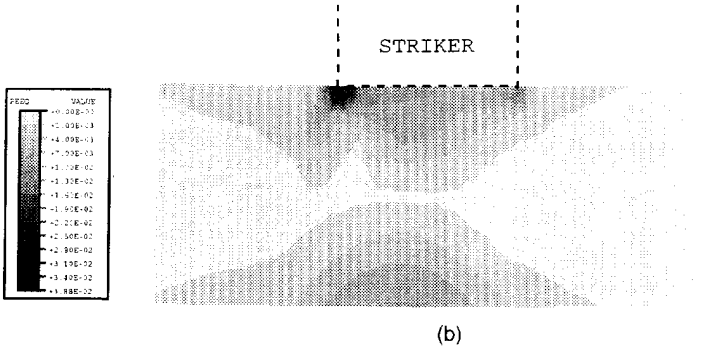

(b)

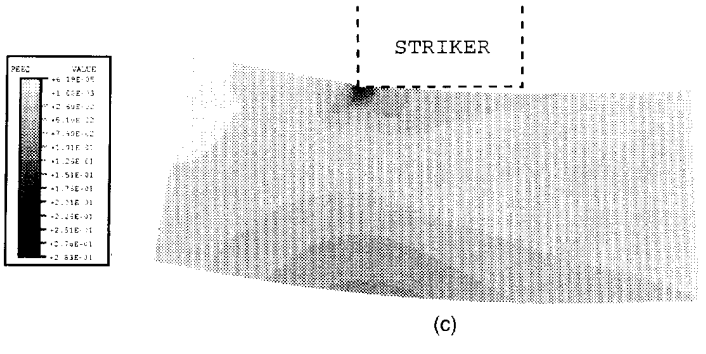

(c)

Fig. 17.

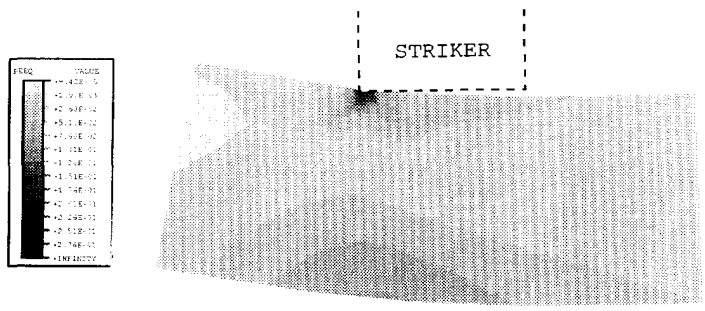

(d)

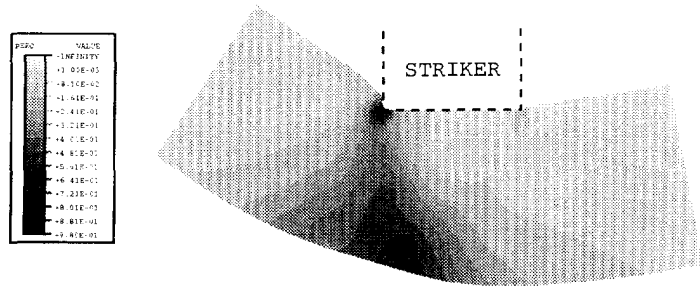

(e)

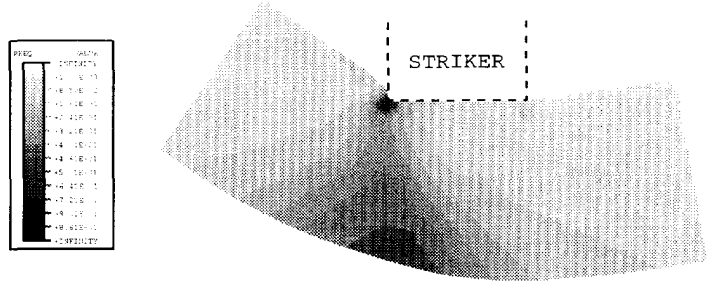

(f)

Fig. 17. Contour of equivalent plastic strain for specimen SB03 (quasi-static) and SB07 (dynamic). (a) SB03, $W = 0.42$ mm; (b) SB07, $W = 0.42$ mm; (c) SB03, $W = 4.42$ mm; (d) SB07, $W = 4.42$ mm; (e) SB03, $W = 15.02$ mm; (f) SB07, $W = 15.02$ mm.

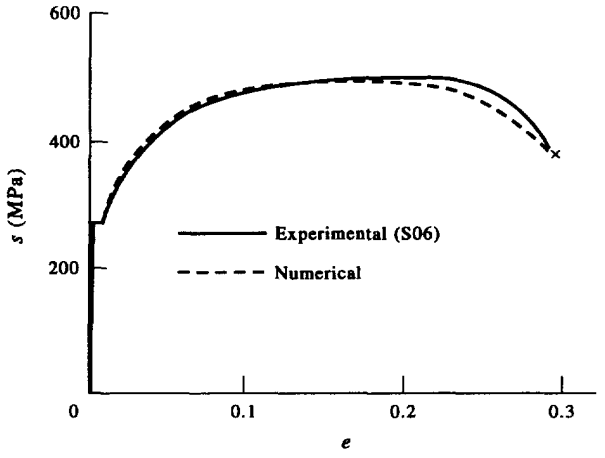

Fig. 6. Comparison of the engineering stress–strain curve for specimen S06 with the numerical prediction for $\dot{\varepsilon} = 0.0012\ s^{-1}$.

with the cross-sectional area at failure, from the actual value comes from the three-dimensional effect. Since both effects were not considered in the data processing of the experimental test results reported by Yu and Jones (1991), the rupture stress and the strain hardening effect beyond the UTS used in the numerical simulation were overestimated. The corrections for the three-dimensional effect evaluated according to Bridgman's formula (Bridgman, 1952), using the shape of the neck obtained numerically, are 6.8% and 6.5% for $\dot{\varepsilon} = 0.0012\ s^{-1}$ and $\dot{\varepsilon} = 0.012\ s^{-1}$, respectively. In comparison with the numerical results, Bridgman's correction appears quite reasonable, though a slight underestimate. For the numerical calculations in this paper the experimental data have been used directly from Yu and Jones (1991) without any corrections.

The distribution of the plastic strain energy density at failure in the necked region is shown in Fig. 5. It transpires that the three-dimensional effect is significant but the change of the strain energy density along the axial direction is rather smooth.

Figure 6 shows a comparison of the engineering stress–strain curve obtained experimentally with that obtained numerically for a strain rate of $0.0012\ s^{-1}$. It should be noted that the numerical curve is sensitive to the magnitude of initial imperfections. A decrease of 17% from $e_f = 0.274$ to $e_f = 0.228$ in the engineering rupture strain is found when the initial reduction of the cross-section radius increases from 1 μm to 8 μm, though the true rupture stress calculated using the one-dimensional theory only increases 0.8% due to an increase of the 3-D effect. Therefore, it is evident that the engineering strain after necking is meaningless even for comparison purposes since it depends not only on the gauge length but also on the magnitude of the initial imperfections.

4. COMPARISON BETWEEN NUMERICAL AND EXPERIMENTAL RESULTS FOR BEAMS

Table 2 contains a comparison of the transverse displacements for dynamically loaded steel beams obtained numerically with the corresponding experimental data. The agreement

Table 2. Numerical and experimental results for the transverse displacement of dynamically loaded mild steel beams

Specimen	Numerical	Experimental†	Comments on tests
SB09	$W_p = 20.56$ mm	$W_p = 20.9$ mm	
SB08	$W_{max} = 21.26$ mm	$W_f = 21.8$ mm	just broken
SB06	$W_{max} = 22.80$ mm	$W_f = 22.8$ mm	broken
SB07	$W_p = 14.97$ mm	$W_p = 14.5$ mm	crack and severe necking
SB05	$W_{max} = 16.03$ mm	$W_f = 15.0$ mm	broken
SB04	$W_{max} = 17.34$ mm	$W_f = 16.0$ mm	broken

†See Yu and Jones (1991).

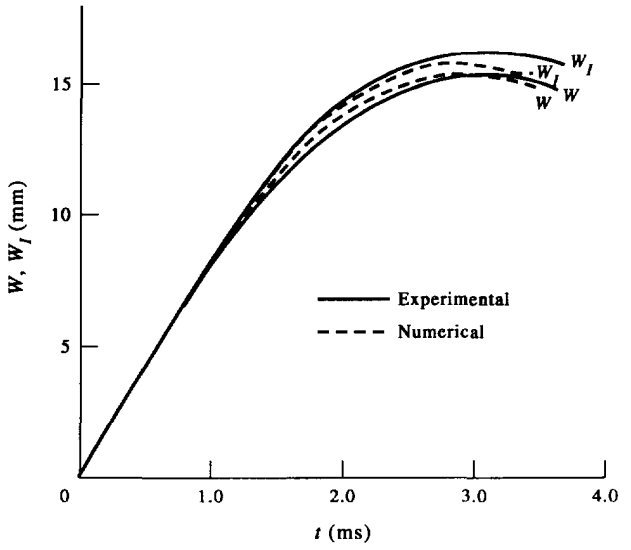

Fig. 7. Deflection-time history for specimen SB07.

between the numerical results and the experimental data is quite reasonable, particularly when considering that the values of W_f were obtained with a limited temporal and spatial resolution of the high-speed photographs.

The calculated deflection-time history for specimen SB07, which was loaded dynamically at the one quarter-span position and was observed to be cracked and severely necked after a test, is compared with the experimental curves in Fig. 7. Excellent agreement is observed. The numerical and experimental load versus displacement curves for the two quasi-static tests, i.e., specimens SB10 and SB03, are shown in Figs 8(a) and (b), respectively. It is found that the numerical curves are slightly higher than the corresponding experimental ones. This is due to the fact that the rupture stress and the strain hardening effect beyond the UTS were overestimated in the material data, as mentioned earlier.

Engineering strain-time histories were recorded by strain gauges during the early stage of motion in Yu and Jones (1991) for specimens SB08 and SB05, which were loaded dynamically at the mid-span and the one quarter-span position, respectively. In order to make a valid comparison, the strain gauge output in the numerical simulations is estimated by averaging the strain over the gauge length, which includes 11 nodes. The comparisons are plotted in Figs 9(a) and (b) for specimens SB08 and SB05, respectively. It is found that the experimental curves are lower than the numerical ones at the early stage ($t < 0.25$ ms), presumably due to imperfections in the impact surface. Similar comparisons for the strain gauge records in the quasi-static cases, i.e., specimens SB10 and SB03, are shown in Figs 9(c) and (d), respectively. During the test of specimen SB03, the loading position moved 0.4 mm towards the mid-span and to estimate this effect, the calculated strain gauge record for a beam loaded $l_1 = 25.4 + 0.635$ mm† is also shown in Fig. 9(d).

The indentation of those specimens, which were not broken after tests, was measured as the difference between the thickness at the indented section and a nearby section using a vernier calliper. However, it is difficult to give an exact definition of the indentation in a numerical simulation. In order to compare with the experimental data, two different measurements, as shown in Fig. 10, are used to obtain a rough estimate. One is the difference between the minimum thickness and that at one element length from the impact point. The other is the distance between the impact point and a straight line which coincides to the nearly undeformed upper surface outside the impact area. It is expected that the former will give an upper bound while the later a lower bound. Good agreement is found for specimen SB09, as shown in Table 3. However, the indentation of specimen SB07 is larger than both of the numerical predictions and it is believed that this occurs because the specimen has already cracked and severely necked, as noted in Table 2.

† The impact position of the striker can only be moved by multiples of the element length which is 0.635 mm.

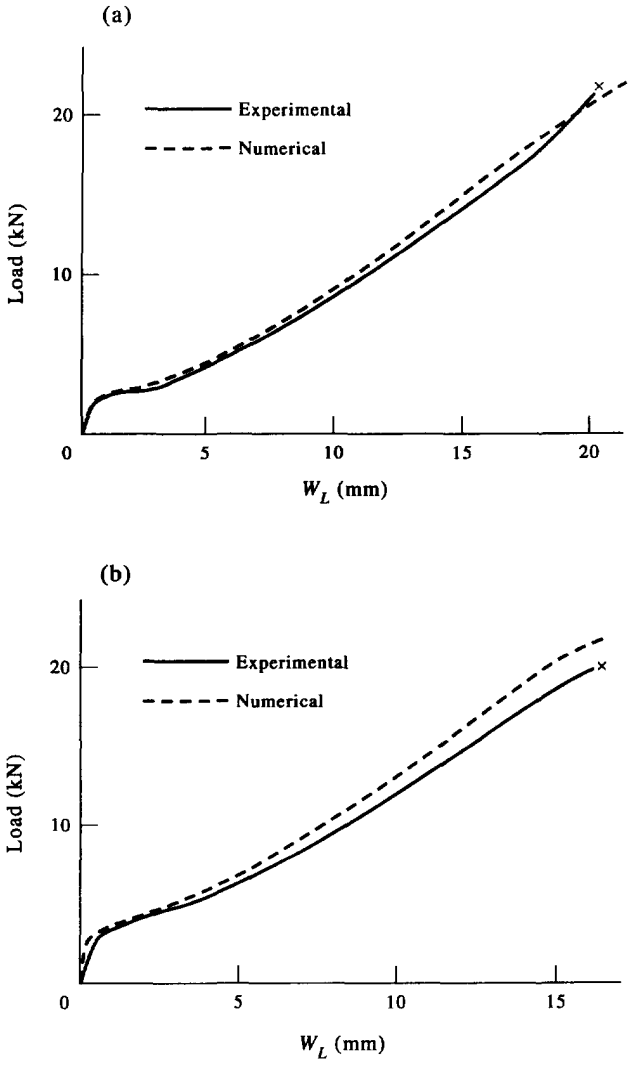

Fig. 8. Load vs displacement curves for (a) specimen SB10 which was loaded quasi-statically at the mid-span, and (b) specimen SB03 which was loaded quasi-statically at the one quarter-span position.

5. MAIN OBSERVATIONS

Table 4 summarizes the critical values of transverse displacement, the maximum strain rate during the main response (excluding the early stage), and the corresponding strain-rate hardening factor defined by

$$\alpha = 1 + (\dot{\varepsilon}/D)^{1/P}, \tag{2}$$

which are obtained by numerical simulation for the beam specimens under impact loading reported by Yu and Jones (1991). As noted earlier, the numerical calculations are undertaken under the assumption that the specimens remained intact and were not broken or damaged during the response. It is observed that the response duration, T, i.e., the time when the maximum deflection was reached, is nearly independent of the impact velocity, as shown in Table 4. The numerical values of α are 1.062 and 1.064 for the quasi-static tests on specimens SB10 and SB03, respectively, according to the strain rate calculated at the failure point in the experiments. Thus, a difference of about 20% in stress is expected between the beams loaded dynamically and those loaded statically, when using a simple estimate of the strain-rate effect.

5.1. *Flexural wave in the early stage of motion*

The distribution of the bending moment for specimen SB08 during the first 100 μs is plotted in Fig. 11, which shows the dispersive nature of an elastic–plastic flexural wave. While the maximum bending moment remains stationary at the impact point, a minimum bending moment with a peak value about $-M_0$ moves towards both supports immediately after impact, which is similar to traveling plastic hinges in the rigid-perfectly plastic model (Jones, 1989a). However, the bending moment ahead of the minimum moment differs from the simple model. Moreover, there is no evidence that a plastic hinge accompanies the movement of the minimum bending moment and maximum curvature. In fact, the beginning of the response is mainly elastic, and only a small amount of plastic deformation occurs near the upper and lower surfaces, as a result of the strain-hardening effect.

Due to the effect of wave dispersion, the higher frequency components travel faster than the lower frequency ones. Another peak, which is less than M_0, has already moved out of the main disturbance a few microseconds after impact. The speed of the maximum and minimum values reduces with time, as a result of wave dispersion. The propagation of the negative peak is further delayed after $t = 20$ μs when the small peak maximum wave has reflected from the support and interacts with the remainder of the wave. Actually, this minimum staggers in the region of 28 mm $< x <$ 38 mm for about 20 μs, resulting in a region of significant plastic bending deformation there. At a later time, after $t > 45$ μs, the

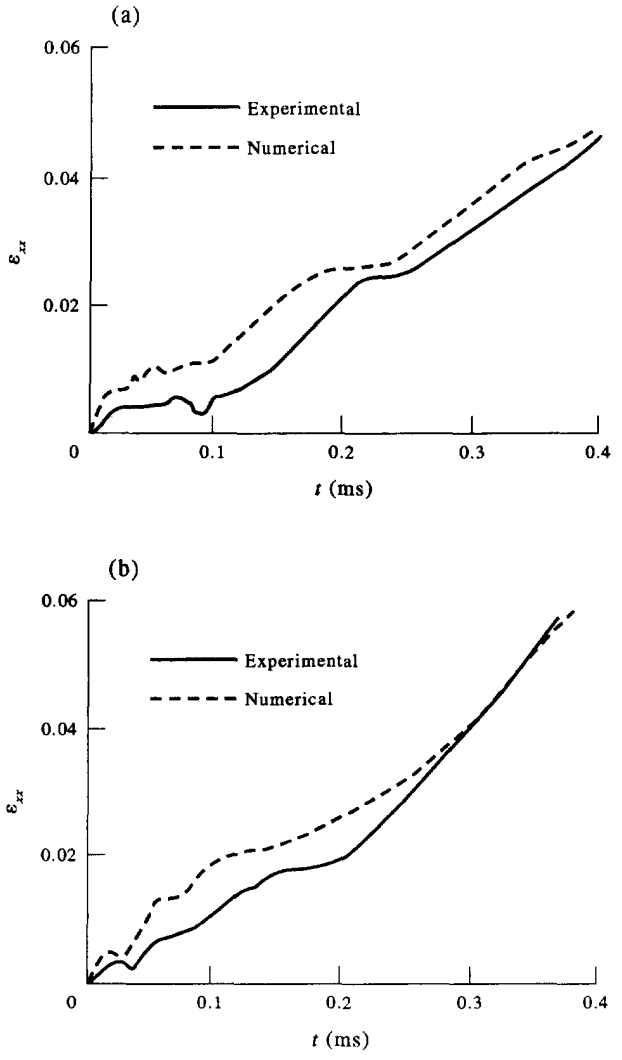

Fig. 9.

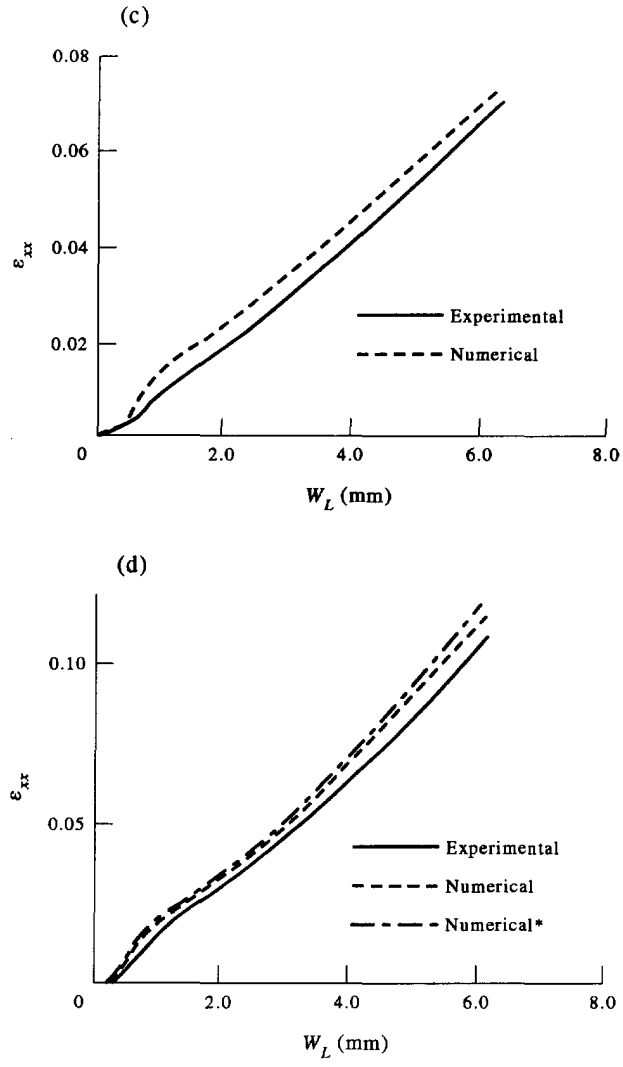

Fig. 9. Comparison of the experimental strains on the lower surface underneath the striker and the numerical prediction across the strain gauge length of 3.81 mm for (a) specimen SB08, (b) specimen SB05, (c) specimen SB10, and (d) specimen SB03 (*: load position moved 0.635 mm towards the mid-span).

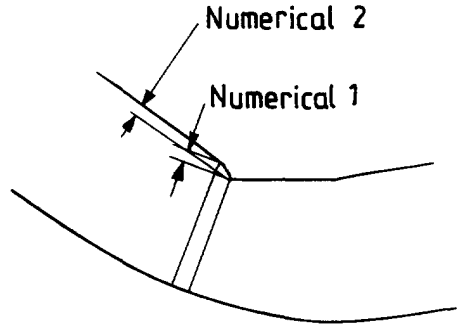

Fig. 10. Two definitions of indentation.

bending moment at the support reaches $-M_0$. The phenomenon then becomes more complicated. A comparison of the time history of the first negative peak value, obtained from the numerical simulation, with the prediction of the rigid-perfectly plastic model, is shown in Fig. 12. It is interesting to note that, while the propagating velocity of the peak

Table 3. Comparison of indentation measured after tests with numerical results

Specimen	Experimental†	Numerical 1	Numerical 2
SB09	0.5 mm	0.68 mm	0.44 mm
SB07	1.1 mm	0.79 mm	0.48 mm

†See Yu and Jones (1991).

Table 4. Calculated maximum displacement and strain rate

Specimen load position comments on tests (Yu and Jones, 1991)	SB09 mid-span	SB08 mid-span just broken	SB06 mid-span broken	SB07 quarter-span crack and necking	SB05 quarter-span broken	SB04 quarter-span broken
H (mm)	6.29	6.20	6.20	6.20	6.23	6.30
B (mm)	10.10	10.13	10.16	10.17	10.06	10.18
l_1 (mm)	50.5	49.9	50.8	25.4	25.4	25.4
V_0 (m/s)	10.5	10.6	11.5	8.8	9.2	10.1
T (ms)	3.27	3.28	3.28	2.86	2.86	2.85
W (mm)	20.93	21.26	22.81	15.31	16.03	17.34
W_t (mm)				15.02	15.72	16.98
W_l (mm)	21.81	22.14	23.93	15.61	16.38	17.79
W_p (mm)	20.56	20.88	22.45	14.97	15.70	17.03
$\dot{\varepsilon}$ (s^{-1})†	310	325	370	240	260	345
α	1.2846	1.2862	1.2907	1.2760	1.2786	1.2883

†Higher values exist during the early stage of the response due to the stress wave effect.

is quite different from the prediction of the rigid-perfectly plastic theory, this theory gives a reasonable prediction for the location of the peak value before wave interaction. This phenomenon was also examined by Reid and Gui (1987) who used beam elements and an elastic-perfectly plastic material model. It was found that the distributions of the bending moment before wave reflection were similar to the elastic solution and the location of the peak values could be predicted by the rigid-perfectly plastic model quite accurately. However, they also found that full plasticity was achieved only over small regions of the beam.

It is expected that more maxima and minima will occur at later times and propagate with higher velocity but smaller amplitude, which will, more or less, affect the bending moment distribution. This can be seen clearly in Fig. 13, where the history of the bending moment at Section A, defined in Fig. 1, is shown during the first 150 μs. According to the Timoshenko theory, an elastic flexural wave with a wave length of 20 mm, which is similar to that of the main traveling maximum value shown in Fig. 11, will propagate in the same beam at a velocity of 1880 m/s and, when reflected from the support at 22 μs, reach the impact point again at $t = 53$ μs. This agrees well with the main drop of the bending moment at Section A.† It is found that the beam and the striker separated during the time periods $40\ \mu s < t < 45\ \mu s$ and $50\ \mu s < t < 100\ \mu s$. Presumably, the loss of contact between the striker and the beam could also be attributed to this effect, though it is difficult to give a clear description due to the wave interaction.

It is found that after $t = 100$ μs the influence of the flexural wave on the distribution of the bending moment decreases significantly.

5.2. *Deformation and distribution of stress, strain and strain energy density*

Figure 14 shows the axial strain distribution, ε_{xx}, along the upper surface, centroidal axis and the lower surface for specimen SB07 at $t = T$. It transpires that the bending deformations are concentrated near to the impact point and the support, especially during the later stage of the response when it occurs within regions within a distance H from the impact point or the support. The axial strain in the shorter section of the beam increases more rapidly than that in the longer section and, finally, it is approximately twice as large.

† Only a very small part of the beam undergoes plastic deformation during this stage which has a minor influence on the elastic wave propagation.

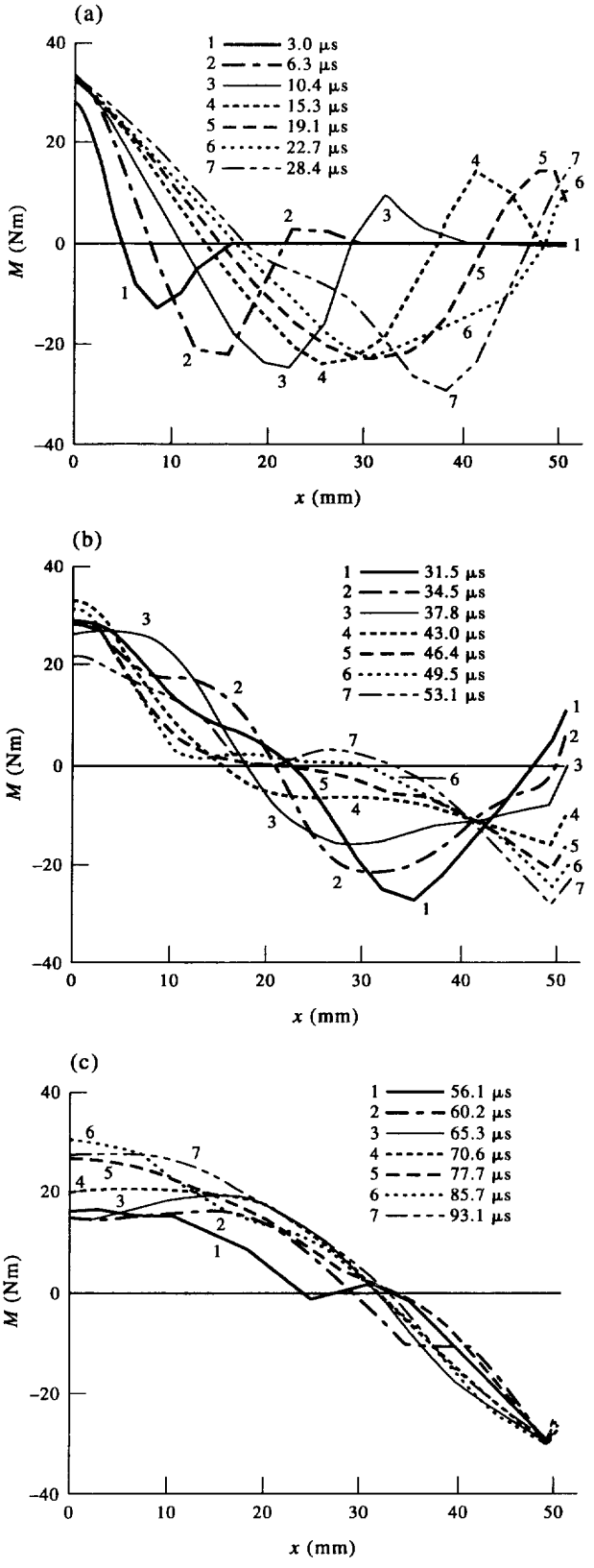

Fig. 11. Distribution of the bending moment during the first 100 μs of the response for specimen SB08.

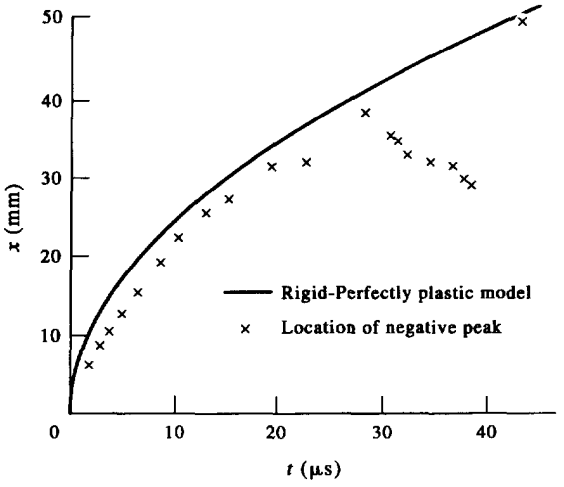

Fig. 12. Comparison of the time history on the first negative peak value of the bending moment with the prediction of the rigid-perfectly plastic model (equation (3.91) in Jones, 1989a).

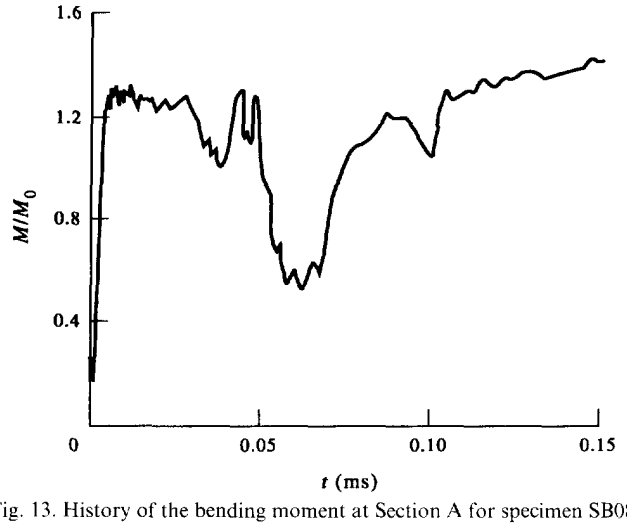

Fig. 13. History of the bending moment at Section A for specimen SB08.

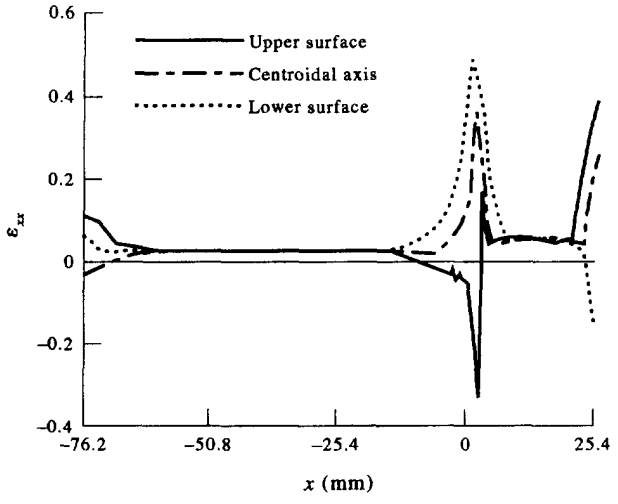

Fig. 14. Distribution of the axial strain along the upper surface, centroidal axis and the lower surface for specimen SB07 at $t = 2.86$ ms.

This is in good agreement with the measured thickness differences in the two sections after a test. It is found that the membrane strain is significant when $t > 0.5$ ms ($W > H$).

The maximum values of the tensile stress and strain are located on the lower surface underneath the striker, at the symmetric axis for the specimens impacted at the mid-span (node 17), or slightly towards the support for those impacted at the one-quarter span position (node 1017), where necking or a tensile tearing failure takes place. On the other hand, the maximum values of the Mises stress, Tresca stress, shear strain, equivalent plastic strain and plastic strain energy density occur on the upper surface, at the impact point (node 161 or node 1121), or near this point (node 163 or nodes 1101, 1123) where a shear failure takes place. The distributions of the Mises stress, equivalent plastic strain and plastic strain energy density for specimen SB07 at $t = T$ are shown in Fig. 15. It transpires that the equivalent plastic strain and the plastic strain energy density are concentrated near the impact point, in contrast with the smooth change along the axial direction found in the neck region of the tensile specimens, as shown in Fig. 5.

A high strain gradient is observed along the length of a strain gauge located underneath the striker (gauge length 3.81 mm), especially during the second half of the response. At the time when the maximum deflection is reached, the strain at the centre of a gauge is about twice as large as that at the edge of the gauge.

The distribution of the Tresca stress along the ridge of the Tresca stress contour across the beam thickness tends to be uniform at the later stage of the response except in a region very near to the impact point, as shown in Fig. 16. The angle of the ridge of the Tresca stress contour is coincident with the fracture or sliding surface observed in the dynamic tests reported by Yu and Jones (1991), indicating that failure develops along the direction of the maximum shear stress.

5.3. *Inertia effect and strain-rate effect*

A comparison of the equivalent plastic strain distributions for specimens SB07 (dynamic) and SB03 (quasi-static) is shown in Fig. 17. At an early stage of the response, the stress wave effect (inertia effect) is significant in the dynamic tests. In comparison with the quasi-static case for the same transverse deflection, the size of the plastic region is larger and the plastic strain is higher, as shown in Figs 17(a) and (b) for $W = 0.42$ mm. After a few hundred microseconds, the plastic deformation in the dynamically loaded specimen is similar to that under a quasi-state loading, as shown in Figs 17(c) and (d) ($W = 4.42$ mm). However, the plastic strain increases more rapidly with the increase of transverse deflection in a quasi-static test than in the dynamic test, as indicated in Figs 17(e) and (f) ($W = 15.02$ mm). Furthermore, there is some evidence in this figure that the beam under a quasi-static loading tends to neck (geometrical instability), which may account for the rapid increase of the plastic strain. In comparison, this phenomenon occurs later for beams under an impact loading, probably due to the inertia effect. It is not clear whether or not this is also due to the strain-rate effect, which is included in both the quasi-static and dynamic simulation, but is more significant for impact loading.

The stress, strain and plastic strain energy density versus transverse deflection curves for beams struck with masses having different velocities are nearly coincident, indicating the feasibility of using a single stress–strain curve for all dynamic tests within the impact velocity range studied in this paper. However, the quasi-static curves differ from the corresponding dynamic one significantly, as shown in Fig. 18. If the strain-rate hardening effect is taken into account, it is expected from eqn (2) that the stress in the dynamic case should be about 21% larger than that in a quasi-static case. This is in agreement with the numerical results for the deflection range between 1 and 15 mm. However, a similar increase in the plastic strain energy density is not found because the plastic strain in the quasi-static case, as mentioned above, increases more rapidly than in the dynamic case. This compensates somewhat for the smaller strain energy density because of the less significant strain-rate hardening effect. For example, at $W_L = 15$ mm, the plastic strain of specimen SB10 (static) is 11.5% larger than that for specimen SB08 (dynamic), leading to a stress in specimen SB08 only 5.5% larger than that in specimen SB10. A similar phenomenon is also found for the specimens loaded at the one quarter-span position.

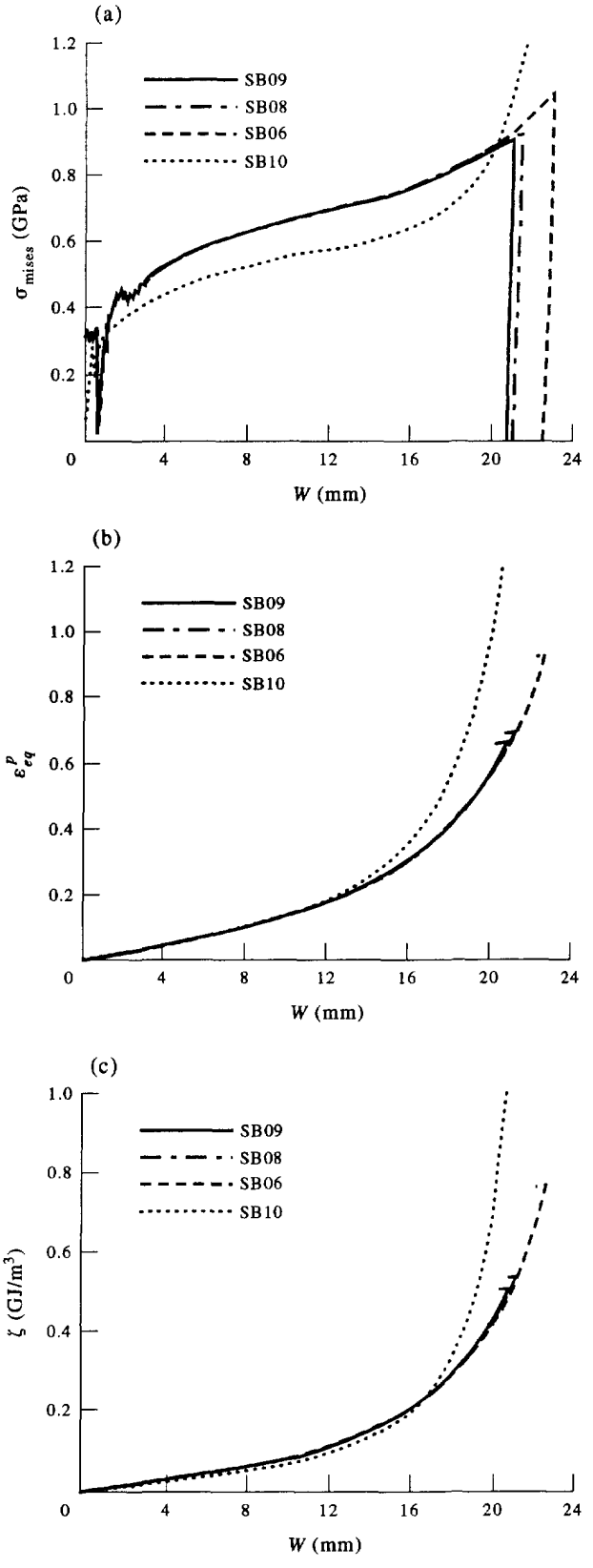

Fig. 18. (a) Mises stress, (b) equivalent plastic strain, and (c) plastic strain energy density, at the lower surface underneath the striker versus the transverse deflection for beams loaded at the mid-span.

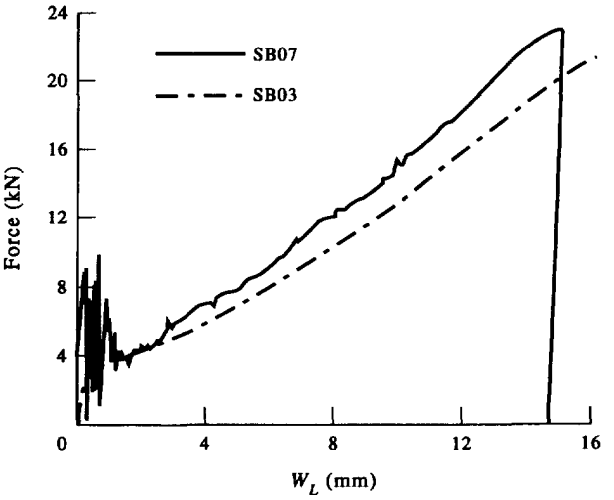

Fig. 19. Comparison of the interfacial forces for specimens SB07 and SB03.

A comparison of the interfacial force versus the transverse deflection curves for the dynamic (SB07) and quasi-static (SB03) cases is shown in Fig. 19. It is observed that the interfacial force in the dynamic case is about 16% larger than that in the quasi-static case, in contrast with an approximate difference of 20% between the strain-rate hardening effects using the maximum strain-rate for the two cases.

6. DISCUSSION ON FAILURE CRITERIA FOR BEAMS

It is possible to examine the detailed information on the response of the beams and explore the accuracy of various dynamic inelastic failure criteria (within the framework of classical continuum mechanics). However, it is necessary to specify the requirements for identifying a failure criterion according to the final condition of the beams examined experimentally in Yu and Jones (1991).

In the experimental study, it was found that necking was located on the lower surface, while a crack initiated at the impact point on the upper surface. Hence we should consider the quantities on the lower surface as candidates for the criterion of tensile failure and those on the upper surfaces as candidates for the criterion of shear failure.† Since specimen SB07 was cracked and severely necked, it is natural to choose the maximum (or minimum) value for this specimen as the critical value for predicting both tensile and shear failures.

For a tensile failure criterion, it is necessary that

$$V_{SB09} < V_{SB07} < V_{SB06}, \tag{3}$$

where V denotes the critical (absolute) value used in the criterion, since specimen SB06 was broken, while specimen SB09 was not. Furthermore, it is desirable that the value for specimen SB07 should be less than, or at least close to, that for specimen SB08 which has just broken.

It is found that the hydrostatic pressure near to the impact point during the final stage of the response for those specimens impacted at the one quarter-span position is about double for those specimens impacted at the mid-span, as shown in Table 6. Generally speaking, material ductility increases with an increase of the hydrostatic pressure and the failure strain is a function of the stress triaxiality.‡ Hence, it is expected that the specimens impacted at the one quarter-span position can withstand a higher strain without failure than those beams impacted at the mid-span. It is also believed that specimen SB08 was not

† Some quantities near to the impact point are mesh-dependent. However, when the same mesh is used in this region, any comparisons are still meaningful.

‡ Although plastic deformation and the plastic strain energy density are deviatoric quantities and independent of the hydrostatic pressure, the failure strain is affected by the magnitude of the hydrostatic pressure.

Table 5. Critical values related to tensile tearing failure†

Specimen	SB09	SB08	SB06	SB07	SB05	SB04	Comments‡
ε_{xx} (node 17/1017)	0.6624	0.6912	0.9245	0.4867	0.5494	0.7173	B
$\varepsilon_{xx}/\varepsilon_f$ (node 17/1017)	0.7981	0.8328	1.1139	0.5864	0.6619	0.8666	
ε^p_{eq} (node 17/1017)	0.6582	0.6870	0.9200	0.4829	0.5455	0.7150	B
$\varepsilon^p_{eq}/\varepsilon_f$ (node 17/1017)	0.7930	0.8277	1.1084	0.5818	0.6572	0.8614	
σ_{xx}/σ_y (node 17/1017)	3.487	3.538	3.962	3.161	3.278	3.599	B
σ_{xx}/σ_f (node 17/1017)	1.152	1.169	1.309	1.044	1.083	1.189	
$\sigma_{xx}/\alpha\sigma_f$ (node 17/1017)	0.897	0.908	1.014	0.818	0.847	0.923	
σ_{Mises}/σ_y (node 17/1017)	3.484	3.537	3.971	3.158	3.276	3.604	B
σ_{Mises}/σ_f (node 17/1017)	1.151	1.168	1.312	1.043	1.082	1.190	
$\sigma_{Mises}/\alpha\sigma_f$ (node 17/1017)	0.896	0.908	1.016	0.817	0.846	0.924	
N/N_0 (Section A)	2.367	2.392	2.636	1.959	2.026	2.140	
$N/\alpha N_0$ (Section A)	1.843	1.860	2.042	1.535	1.585	1.661	
N/N_f (Section A)	0.782	0.790	0.871	0.647	0.669	0.707	
N/N_0 (Section B)	2.307	2.339	2.488	2.390	2.477	2.662	
$N/\alpha N_0$ (Section B)	1.796	1.818	1.928	1.873	1.937	2.066	
N/N_f (Section B)	0.762	0.773	0.822	0.789	0.818	0.879	
M/M_0 (Section A)	1.586	1.572	1.597	1.751	1.760	1.770	A and C
$M/\alpha M_0$ (Section A)	1.235	1.222	1.237	1.372	1.376	1.374	
M/M_f (Section A)	0.524	0.519	0.527	0.578	0.581	0.585	
M/M_0 (Section B)	1.587	1.571	1.595	1.811	1.817	1.820	
$M/\alpha M_0$ (Section B)	1.235	1.221	1.236	1.419	1.421	1.413	
M/M_f (Section B)	0.524	0.519	0.527	0.598	0.600	0.601	

†All values are the maximum values reached during the response.
‡Definition of the symbols:
A—Not suitable for a failure criterion because it is evaluated during the early response;
B—Not suitable for a failure criterion because the value for specimen SB07 is less than that for specimen SB09;
C—Not suitable for a failure criterion because the value for specimen SB07 is larger than that for specimen SB06.

broken in the shear mode and, as noted earlier, the extrapolated stress and strain values at the impact point contain inaccuracies due to the limitations of Gaussian integration. In considering the above facts, less experimental data is available for obtaining a shear failure criterion than is available for a tensile failure. The main requirement is that

$$V_{\mathrm{SB09}} < V_{\mathrm{SB07}}, \tag{4}$$

otherwise specimen SB09 would have broken in a shear mode.

Only those variables which reach their maximum/minimum values at or near the time when the maximum deflection is reached need to be considered.

6.1. *Criteria based on stress, strain or generalised stress and strain*

Let us first consider the possibility of using a single parameter, such as stress or strain at the material level, and bending moment, shear force or membrane force at the structural level, as a failure criterion. The numerical results related to a tensile tearing failure and a shear failure are listed in Tables 5 and 6, respectively. It transpires that only the maximum membrane force (or N/N_0) for a tensile failure criterion and the maximum Tresca or Mises stress for a shear failure are worthy of further consideration.

Besides the above one-parameter criteria, which are mainly local in nature, it is also possible to consider other criteria with more parameters or mixed with some global quantities. The advantage of such criteria is the possibility of predicting both tensile and shear failures and more complex failure modes.

6.2. *Criterion based on global deformations*

The maximum tensile strain curves for the two sets of specimens loaded dynamically, when plotted against the overall rotation angle defined by Yu and Jones (1989), are very close, as shown in Fig. 20. However, it appears that a critical overall rotation angle for a tensile failure, which was valid for the aluminium alloy beams as reported by Yu and Jones

Table 6. Critical values related to shear failure†

Specimen	SB09	SB08	SB06	SB07	SB05	SB04	Comments‡
ε_{xy} (node 163/1123)	−0.3331	−0.3318	−0.3333	−0.4361	−0.4413	−0.4477	C
$\varepsilon_{xy}/\varepsilon_f$ (node 163/1123)	−0.4013	−0.3998	−0.4016	−0.5254	−0.5317	−0.5394	
ε^p_{eq} (node 161/1121)	0.9664	1.028	1.473	0.9115	1.071	1.504	B
$\varepsilon^p_{eq}/\varepsilon_f$ (node 161/1121)	1.1643	1.2386	1.7747	1.0982	1.2904	1.8120	
σ_{xy}/τ_y (node 203/1163)	−2.324	−2.310	−2.328	−2.814	−2.824	−2.848	A
σ_{xy}/τ_f (node 203/1163)	−0.786	−0.763	−0.769	−0.929	−0.933	−0.941	
$\sigma_{xy}/\alpha\tau_f$ (node 203/1163)	−0.598	−0.593	−0.596	−0.728	−0.729	−0.730	
σ_{Mises}/σ_y (node 161/1101)	3.912	3.967	4.517	3.997	4.010	4.047	
σ_{Mises}/σ_f (node 161/1101)	1.292	1.310	1.492	1.320	1.324	1.337	
$\sigma_{Mises}/\alpha\sigma_f$ (node 161/1101)	1.006	1.019	1.156	1.035	1.036	1.038	
σ_{Tresca}/σ_y (node 161/1101)	4.497	4.547	5.046	4.550	4.564	4.609	
σ_{Tresca}/σ_f (node 161/1101)	1.485	1.502	1.667	1.503	1.507	1.522	
$\sigma_{Tresca}/\alpha\sigma_f$ (node 161/1101	1.156	1.168	1.291	1.178	1.179	1.182	
Q/Q_0 (Section B, 2.8 μs)	−0.919	−0.927	−0.942	−0.895	−0.897	−0.911	A
$Q/\alpha Q_0$ (Section B, 2.8 μs)	−0.715	−0.721	−0.730	−0.701	−0.702	−0.707	
Q/Q_f (Section B, 2.8 μs)	−0.304	−0.306	−0.311	−0.296	−0.296	−0.301	
Q/Q_0 (Section B, later)	−0.393	−0.392	−0.395	−0.503	−0.503	−0.510	
P/σ_y (node 141/1101)	2.092	2.087	2.096	2.554	2.570	2.597	—
P/σ_y (node 141/1101, $t = T$)	0.871	0.842	0.619	1.683	1.572	1.215	

†All values are the maximum/minimum values reached during the response unless otherwise noted.
‡Definition of the symbols:
A—Not suitable for a failure criterion because it is evaluated during the early response;
B—Not suitable for a failure criterion because the value for specimen SB07 is less than that for specimen SB09;
C—Not suitable for a failure criterion because the value is insensitive to the impact velocity.

(1989), does not exist for the mild steel specimens since the maximum tensile strain at failure for the two sets of specimens is different.

6.3. *Criterion based on an interaction yield surface*

According to the interaction yield surface suggested by Sobotka (1955), we introduce a yield index defined by

$$\xi = |M/M_0|\sqrt{1-(Q/Q_0)^2}+(N/N_0)^2+(Q/Q_0)^2. \tag{5}$$

A failure index, ξ_f, is also obtained by replacing σ_y with σ_f in the calculations for M_0, N_0 and Q_0 in eqn (5). The maximum values of ξ and ξ_f reached during the dynamic response

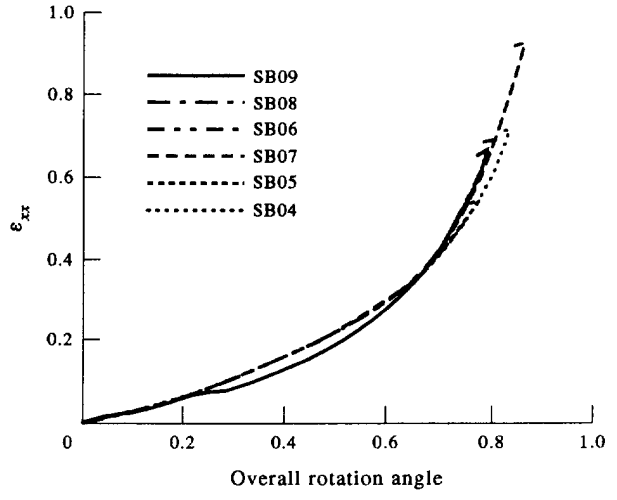

Fig. 20. Variation of the maximum tensile strain with overall rotation angle for the beams under impact loading.

Table 7. Critical values of the yield and failure indices†

Specimen	SB09	SB08	SB06	SB07	SB05	SB04
ξ	6.540	6.668	7.957	6.330	6.695	7.419
ξ_f	0.921	0.934	1.091	0.911	0.946	1.063

†All values are the maximum values reached during the response.

are listed in Table 7. It is found that the maximum values occur at section A for the specimens impacted at the mid-span. However, for the specimens loaded at the one quarter-span position, the maximum values of ξ and ξ_f are located between Section A and B with a distance of 0.635 mm and 1.27 mm from the impact point for ξ and ξ_f, respectively. These results are promising for a suitable failure criterion. It is interesting to note that when the load position moves from the mid-span to the one quarter-span position, there is a transition of the maximum value of ξ from Section A towards Section B, with a concomitant tendency for a shear failure.

6.4. *Criterion based on the conditions at the fracture surface*

As mentioned earlier, the distribution of the Tresca stress along the ridge of the Tresca stress contour across the beam thickness in Fig. 16 tends to be uniform during the late stage of the dynamic response except in a region close to the impact point. Moreover, the experimental results show that both the tensile and shearing failures propagate along the line where the Tresca stress and hence the maximum shear stress are maximum. In fact, the specimens loaded at the one quarter-span position ruptured due to the combined effect of tensile tearing and shearing. Therefore, a critical value of σ_{Tresca} along this line† (except in a region close to the impact point) may be used to predict both tensile and shear failures. Alternatively, one can use the peak value along, say, the centroidal axis for an approximate criterion. The distribution of the Tresca stress in the vicinity of the peak value along the centroidal axis in the six impact loaded beam specimens in Table 1, at the time when the maximum deflection is reached, are plotted in Fig. 21. These results confirm the validity of this criterion at least for the present test results. The critical value of the Tresca stress on the centroidal axis is found to be 785 MPa when specimen SB07 is assumed to give the critical conditions (note that $\sigma_f = 784$ MPa).

Another parameter, i.e., shear strain along the ridge in Fig. 16, is also worth considering since ductile fracture is dominated by strain rather than stress. Within the framework of finite deformations, however, only the strain increment rather than the strain itself is

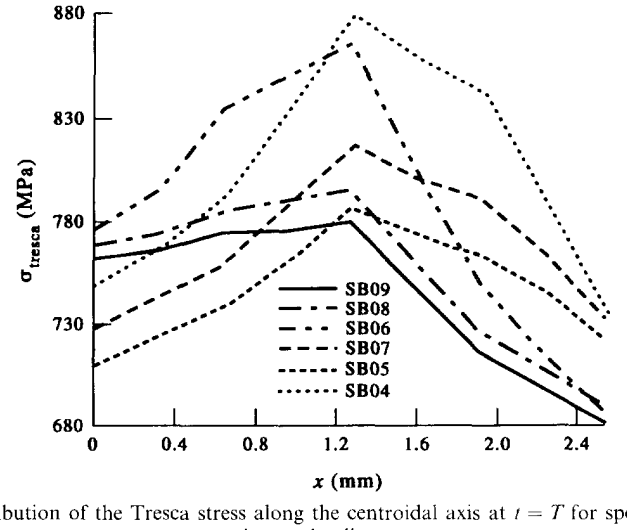

Fig. 21. Distribution of the Tresca stress along the centroidal axis at $t = T$ for specimens under impact loading.

† As mentioned earlier, the distribution of σ_{Tresca} along this line is approximately uniform during the late stage of the dynamic response.

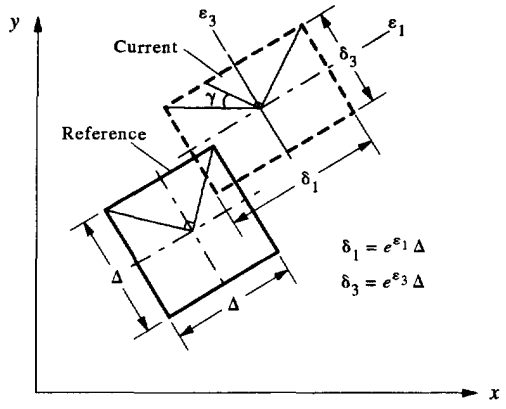

Fig. 22. Definition of γ.

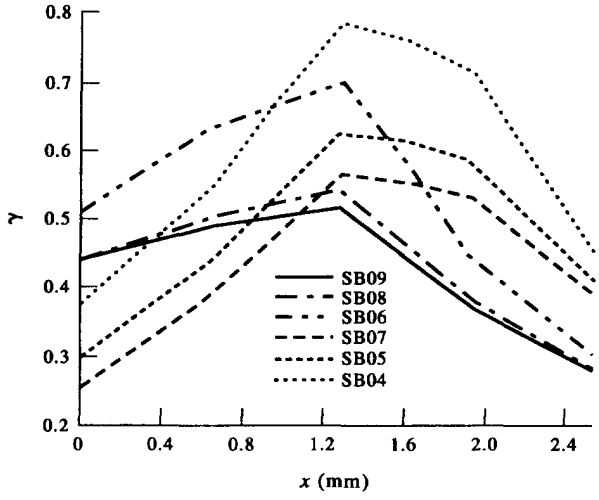

Fig. 23. Distribution of γ along the centroidal axis at $t = T$ for specimens under impact loading.

defined. Nevertheless, the maximum shear strain can be described by the change of the angle between the axes of maximum and minimum principal stretches as

$$\gamma = 2\arctan[(e^{\varepsilon_1} - e^{\varepsilon_3})/(e^{\varepsilon_1} + e^{\varepsilon_3})], \tag{6}$$

where ε_1 and ε_3 are the maximum and minimum principal true strains, respectively, as shown in Fig. 22. The distribution of γ along the centroidal axis, at the time when the maximum deflection is reached in the dynamic tests in Table 1, is shown in Fig. 23. In considering the effect of the hydrostatic pressure, the threshold value of γ will increase with any increase in the hydrostatic pressure. Hence, specimen SB07 could remain at a critical condition, while specimen SB08, though having a lower value of γ, but also a lower hydrostatic pressure, as shown in Table 6, would break. Therefore, it also appears promising to use a critical curve, $\gamma(P)$, to predict the rupture of the beams. Further study, especially to obtain the experimental data for $\gamma(P)$, is required to confirm whether or not this is suitable as a failure criterion.

6.5. *Criterion using strain energy density*

Generally speaking, there are three different approaches for considering a critical value of the strain energy density as a failure criterion. One is at the structural level when the strain energy density is estimated within a plastic hinge, as suggested by Shen and Jones (1992). This method retains the simultaneous influence of the bending moment, membrane force and transverse shear force but depends largely on the selection of an appropriate

Table 8. Critical values of plastic strain energy density†

Specimen	SB09	SB08	SB06	SB07	SB05	SB04
η (node 17/1017)	0.953	1.006	1.457	0.653	0.758	1.061
η/α (node 17/1017)	0.742	0.782	1.129	0.512	0.593	0.824
η (element 5/88)	0.775	0.807	1.084	0.588	0.678	0.927
η/α (element 5/88)	0.603	0.627	0.840	0.461	0.530	0.720
η (node 161/1121)	1.449	1.566	2.489	1.398	1.700	2.628
η/α (node 161/1121)	1.128	1.218	1.928	1.096	1.330	2.040
η (element 16/94)	0.489	0.523	0.794	0.629	0.715	0.952
η/α (element 16/94)	0.381	0.407	0.615	0.493	0.559	0.739

†All values are the maximum values reached during the response.

volume for the plastic hinge and the choice of a critical strain. The other two criteria are at the material level and the strain energy density is evaluated at a point, where the failure is initiated, or over a characteristic volume of material, where damage takes place. Here only the later two approaches are discussed.

The calculated critical values of the non-dimensional plastic strain energy density at the critical points (node 161 or 1121) or at the centroid of the element attached to these points (element 16 or 94) are listed in Table 8. A significant difference is found between the value at node 161 or 1121 and that in the nearby element, element 16 or 94 (dimension 0.635×0.794 mm^2), which indicates a very high strain concentration. It is evidence that the values of the maximum plastic strain energy density on both the upper and the lower surfaces of a beam are not suitable for use as a failure criterion, possibly due to the poor accuracy of the numerical data at the impact point. However, in comparing these data, it is found that the change of the plastic strain energy density near to the impact point is more rapid for the specimens loaded at the mid-span than for those specimens loaded at the one quarter-span position. If the strain energy density is averaged over a characteristic volume or evaluated at a characteristic distance from the impact point, then it is possible that the magnitudes would be more suitable for use as a criterion for predicting shear failure. This volume, according to the data listed in Table 8, appears to be smaller than the element size and a characteristic length scale, λ, may be introduced which is in the order of 100 μm. This value is in agreement with the typical scale of a damaged region in a structure (Lemaitre and Dufailly, 1987).

To make a rough estimate of this characteristic length, we adopt the following assumptions:

1. the distribution of the plastic strain energy density between the impact point and the centroid of the nearby element is linear;
2. failure occurs when the plastic strain energy density, at a characteristic distance from the impact point, reaches a critical value;
3. this critical value is strain-rate insensitive so that $\eta_c = 1$.†

This leads to a characteristic length of $\lambda = 260$ μm, approximately, according to the value for specimen SB07 which is in a critical condition, as shown in Fig. 24. Thus, it appears that this criterion provides a correct prediction for the failure of the beams observed by Yu and Jones (1991). Further investigation is necessary to assess the procedure for choosing a characteristic volume and the critical value of the strain energy density. For example, whether the plastic strain energy density should be evaluated at a characteristic distance from the impact point or averaged within a region with a characteristic length scale; and whether the critical plastic strain energy density is strain-rate sensitive or related to the failure strain.

7. FINAL REMARKS

The numerical simulation is in excellent agreement with the experimental data reported by Yu and Jones (1991) on the impact behaviour of mild steel beams, especially when

† As noted earlier, the plastic strain energy density near the fracture surface of a tensile specimen changes rather smoothly, as shown in Fig. 5. Hence, in this case, its value is insensitive to the characteristic length scale.

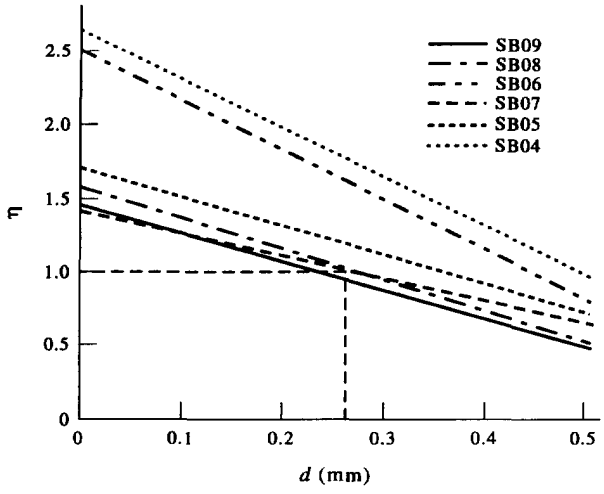

Fig. 24. Estimate of the characteristic length scale for the strain energy density criterion.

considering the fact that there are no adjustable parameters in the specification of the material properties which were obtained experimentally for the same material. Hence, these numerical results, together with the experimental data, provide a reliable set of information for further analysis.

In comparison with the quasi-static loading cases, the stress wave effect is important during the early stage of the response for beams subjected to an impact loading even though the maximum impact velocity is only 8 m/s. The stress also increase in the dynamic cases for materials having a strain-rate hardening effect. Complex failure modes with the combined effects of tensile tearing and shearing, and, possibly, geometrical instability, were obtained experimentally. However, the geometrical instability is delayed by the inertia effect in the dynamic cases.

Among the possible failure criteria discussed in this paper, the maximum membrane force in a beam cross-section appears to be the most promising for a tensile failure, while the maximum Tresca stress or Mises stress and the maximum plastic strain energy density are worthy of further study for a shear failure. The maximum Tresca stress, or shear strain at the centroidal axis, and the maximum yield index, or failure index, defined by eqn (5), are promising parameters for a global failure criterion. Further investigations are required to confirm the reliability of these criteria, especially for predicting a shear failure since only one set of test results, i.e., the beams loaded at the one quarter-span position, are related to shear failure in the experimental study reported by Yu and Jones (1991).

The approach used in the present numerical study provides a critical way to evaluate the reliability and generality of a criterion for predicting the failure of structures subjected to dynamic loads which produce large inelastic strains. The key requirement is a complete set of reliable experimental data including both the structural response and the dynamic properties of the material. Unfortunately, there is a paucity of such data, especially those related to the rupture behaviour of materials under dynamic loading, including the influence of the strain-rate and the hydrostatic pressure. It is clear that further experimental studies and numerical investigations are necessary to achieve a better understanding of the phenomena of structural failure.

Only the criteria based on classical continuum mechanics are discussed in this paper. Recently, some more sophisticated approaches, such as damage mechanics using internal variables or statistical models, have been used for the analysis of structures as well as materials (see, e.g., Tvergaard and Needleman, 1993; Mathur *et al.*, 1994; and Cipollina *et al.*, 1995). These criteria can also be examined using the approach in this paper which involves a partnership between experimental studies and numerical simulations. On the other hand, some empirical or phenomenological failure criteria, such as those sought in this paper, are valuable for engineering design, though the application will be limited.

Acknowledgements—The study reported in this paper was undertaken when the first author (JLY) visited the Impact Research Centre in the Department of Mechanical Engineering at the University of Liverpool. J. L. Yu wishes to express his gratitude to the Royal Society, the Chinese Academy of Sciences and the Impact Research Centre for the financial support of his visit and to the Department of Mechanical Engineering at the University of Liverpool. The computations reported here were done on the Silicon Graphics 12 CPU R4000 system at the University of Liverpool using the ABAQUS code provided by HKS Inc.

REFERENCES

Bridgman, P. W. (1952). *Studies in Large Plastic Flow and Fracture*. McGraw-Hill, New York.

Cipollina, A., López-Inojosa, A. and Flórez-López, J. (1995). A simplified damage mechanics approach to nonlinear analysis of frames. *Computers & Structures* **54,** 1113–1126.

Clift, S. E., Hartley, P., Sturgess, C. E. N. and Rowe, G. W. (1987). Further studies on fracture initiation in plane-strain forging. In *Applied Solid Mechanics*—2 (eds A. Tooth, and J. Spence). Elsevier, Oxford, pp. 89–100.

Clift, S. E., Hartley, P., Sturgess, C. E. N. and Rowe, G. W. (1990). Further prediction in plastic deformation processes. *International Journal of Mechanical Sciences* **32,** 1–17.

Hibbitt, Karlsson and Sorensen, Inc. (1994a). *ABAQUS Theory Manual*, V. 5.4.

Hibbitt, Karlsson and Sorensen, Inc. (1994b). *ABAQUS User's Manual*, V. 5.4.

Jones, N. (1976). Plastic failure of ductile beams loaded dynamically. *Transcriptions of ASME, Journal of Engineering for Industry* **98,** B1, 131–136.

Jones, N. (1989a). *Structural Impact*. Cambridge University Press, Cambridge.

Jones N. (1989b). Recent studies on the dynamic plastic behaviour of structures. *Applied Mechanics Review* **42,** 95–115.

Jones, N. and Wierzbicki, T. (1993). *Structural Crashworthiness and Failure*. Elsevier Applied Science, London and New York.

Lemaitre, J. and Dufailly, J. (1987). Damage measurements. *Engineering Fracture Mechanics* **28,** 643–661.

Mathur, K. K., Needleman, A. and Tvergaard, V. (1994). Ductile failure analyses on massively-parallel computers. *Computer Methods in Applied Mechanics and Engineering* **119,** 283–309.

Menkes, S. B. and Opat, H. J. (1973). Broken beams. *Experimental Mechanics* **13,** 480–486.

Reid, S. R. and Gui, X. G. (1987). On the elastic–plastic deformation of cantilever beams subjected to tip impact. *International Journal of Impact Engineering* **6,** 109–127.

Shen, W. Q. and Jones, N. (1992). A failure criterion for beams under impulsive loading. *International Journal of Impact Engineering* **12,** 101–121.

Shen, W. Q. and Jones, N. (1993a). Dynamic plastic response and failure of a clamped beam struck transversely by a mass. *International Journal of Solids Structures* **30,** 1631–1648.

Shen, W. Q. and Jones, N. (1993b). Dynamic response and failure of fully clamped circular plates under impulsive loading. *International Journal of Impact Engineering* **13,** 259–278.

Sobotka, Z. (1955). *Theorie Plasticity*, t. I-II. CSAV, Praha.

Tvergaard, V. and Needleman, A. (1993). An analysis of the brittle ductile transition in dynamic crack-growth. *International Journal of Fracture* **59,** 53–67.

Yu, J. L. and Jones, N. (1989). Numerical simulation of a clamped beam under impact loading. *Computers & Structures* **32,** 281–293.

Yu, J. L. and Jones, N. (1991). Further experimental investigations on the failure of clamped beams under impact loads. *International Journal of Solids and Structures* **27,** 1113–1137.